

See discussions, stats, and author profiles for this publication at: <https://www.researchgate.net/publication/225592220>

# Microstructure and Low-Cycle Fatigue of a Friction-Stir-Welded 6061 Aluminum Alloy

Article in *Metallurgical and Materials Transactions A* · October 2010

DOI: 10.1007/s11661-010-0279-2

CITATIONS

70

READS

580

3 authors:



A. H. Feng

Tongji University

63 PUBLICATIONS 1,840 CITATIONS

[SEE PROFILE](#)



Daolun Chen

Ryerson University

343 PUBLICATIONS 11,292 CITATIONS

[SEE PROFILE](#)



Z.Y. Ma

Chinese Academy of Sciences

429 PUBLICATIONS 23,421 CITATIONS

[SEE PROFILE](#)

Some of the authors of this publication are also working on these related projects:



Galvanized Autobody Partnership [View project](#)



1. Microstructural control and mechanical behavior of friction stir welded/processed light alloys, supported by the National Natural Science Foundation of China under Grant No. 51331008 [View project](#)

# Microstructure and Low-Cycle Fatigue of a Friction-Stir-Welded 6061 Aluminum Alloy

A.H. FENG, D.L. CHEN, and Z.Y. MA

Strain-controlled low-cycle fatigue (LCF) tests and microstructural evaluation were performed on a friction-stir-welded 6061Al-T651 alloy with varying welding parameters. Friction stir welding (FSW) resulted in fine recrystallized grains with uniformly distributed dispersoids and dissolution of primary strengthening precipitates  $\beta''$  in the nugget zone (NZ). Two low-hardness zones (LHZs) appeared in the heat-affected zone (HAZ) adjacent to the border between the thermomechanically-affected zone (TMAZ) and HAZ, with the width decreasing with increasing welding speed. No obvious effect of the rotational rate on the LHZs was observed. Cyclic hardening of the friction-stir-welded joints was appreciably stronger than that of base metal (BM), and it also exhibited a two-stage character where cyclic hardening of the friction-stir-welded 6061Al-T651 alloy at higher strain amplitudes was initially stronger followed by an almost linear increase of cyclic stress amplitudes on the semilog scale. Fatigue life, cyclic yield strength, cyclic strain hardening exponent, and cyclic strength coefficient all increased with increasing welding speed, but were nearly independent of the rotational rate. Most friction-stir-welded joints failed along the LHZs and exhibited a shear fracture mode. Fatigue crack initiation was observed to occur from the specimen surface, and crack propagation was mainly characterized by the characteristic fatigue striations. Some distinctive tiremark patterns arising from the interaction between the hard dispersoids/inclusions and the relatively soft matrix in the LHZ under cyclic loading were observed to be present in-between the fatigue striations.

DOI: 10.1007/s11661-010-0279-2

© The Minerals, Metals & Materials Society and ASM International 2010

## I. INTRODUCTION

HEAT-TREATABLE 6xxx-series aluminum alloys, containing magnesium and silicon as major alloying elements, are of particular interest due to their attractive combinations of properties as structural materials for the automotive and aerospace applications, *i.e.*, medium strength, high strength and stiffness-to-weight ratios, formability, fatigue resistance, corrosion resistance, and relatively low cost.<sup>[1–3]</sup> 6xxx-series aluminum alloy accounts for a large percentage of the total aluminum production in the world.<sup>[4]</sup> The application of 6xxx-series aluminum alloy in the aerospace and automotive industries involves welding and joining. It is relatively difficult to weld the aluminum alloys using the fusion welding processes. Friction stir welding (FSW), invented at The Welding Institute (Cambridge, United Kingdom) in 1991, provides a promising solution since it is an environmentally friendly, energy-effective, and versatile solid-state joining technique that offers significant

benefits over conventional joining processes due to the absence of the fusion zone.<sup>[5,6]</sup> This joining technique has been proven to be a good alternative especially for the aerospace materials such as 6xxx-series aluminum alloys.

FSW of aluminum alloys has prompted considerable scientific and technological interest because of the difficulties of ensuring the integrity and reliability of joints of lightweight alloys using traditional fusion welding. The advances in this area over the past nearly two decades have been well documented in several excellent overview articles, *e.g.*, References 6 through 8. Recent research into the FSW or friction stir processing (FSP) of 6xxx-series aluminum alloys includes precipitation sequence,<sup>[9–13]</sup> dislocation density,<sup>[14]</sup> texture,<sup>[15–18]</sup> and mechanical properties.<sup>[19–21]</sup> From an engineering design perspective, fatigue properties of FSW aluminum alloys are of particular importance. This has led to increasing research interest in evaluating the fatigue resistance of friction-stir-welded joints, including stress–number of cycles to failure (S-N) behavior<sup>[22–25]</sup> and fatigue crack propagation behavior.<sup>[6,26–28]</sup> However, studies on the low-cycle fatigue (LCF) behavior of the friction-stir-welded aluminum alloys have been limited,<sup>[29–31]</sup> and they are indeed required by automobile manufacturers to estimate the lifetime of components. The LCFs of friction-stir-welded Al-Mg alloys by Czechowski<sup>[29]</sup> and friction-stir-welded AA6061/Al<sub>2</sub>O<sub>3</sub>p and AA7005/Al<sub>2</sub>O<sub>3</sub>p joints by Ceschini *et al.*<sup>[30,31]</sup> have recently been reported. Our previous work on friction-stir-welded 7075Al-T651 alloy has indicated that cyclic

A.H. FENG, formerly Postdoctoral Fellow, Department of Mechanical and Industrial Engineering, Ryerson University, Toronto, ON M5B 2K3, Canada, is Associate Professor, School of Materials Science and Engineering, Harbin Institute of Technology, Harbin 150001, P.R. China. D.L. CHEN, Professor and Ryerson Research Chair, are with the Department of Mechanical and Industrial Engineering, Ryerson University. Contact e-mail: dchen@ryerson.ca. Z.Y. MA, Professor, is with the Shenyang National Laboratory for Materials Science, Institute of Metal Research, Chinese Academy of Sciences, Shenyang 110016, P.R. China.

Manuscript submitted December 6, 2009.

Article published online June 22, 2010

hardening and fatigue life increased with increasing welding speed, but were only weakly dependent on the pin tool rotational rate; the cyclic hardening of the friction-stir-welded joints exhibited a two-stage character.<sup>[32]</sup> To date, no LCF information of the friction-stir-welded 6xxx-series aluminum alloy is available in the literature.

Although the precipitation-hardened aluminum alloys are readily weldable, FSW resulted in a severely softened region in the heat-affected zone (HAZ),<sup>[33]</sup> which was basically characterized by the dissolution/coarsening of precipitates during the thermal cycle.<sup>[13,15,34]</sup> Liu and Ma proposed a heat source zone-isothermal dissolution layer model to explain the low hardness zones (LHZs).<sup>[35]</sup> It was reported that the tensile fracture path of the welds corresponded to the LHZs.<sup>[35,36]</sup> Although several studies have offered important insights in this regard, it is still unclear how the LHZs and the relevant FSW parameters affect LCF properties, and if there are differences in the cyclic hardening characteristics between the friction-stir-welded 6061Al and 7075Al alloys. The objectives of this study were, therefore, to (1) identify the effect of FSW parameters on the microstructure evolution and LCF properties of the welds, (2) study the detailed characteristics on the LCF fracture surfaces of friction-stir-welded joints using a 3-D fractographic examination, and (3) ascertain the cyclic deformation characteristics of the friction-stir-welded 6061Al-T651 joints.

## II. MATERIAL AND EXPERIMENTAL PROCEDURE

The 6.2-mm-thick commercial 6061Al-T651 rolled plates (400-mm long and 80-mm wide), with a composition (wt pct) of (0.8 to 1.2) Mg, (0.4 to 0.8) Si, 0.7 Fe,

(0.15 to 0.4) Cu, (0.04 to 0.35) Cr, (0.15 to 0.4) Mn, (0.15) Ti, and the balance Al, were friction stir welded along the rolling direction using an FSW machine (China FSW Center, Beijing FSW Technology Ltd., Beijing, China). A steel tool with a shoulder 16 mm in diameter and a cylindrical threaded pin 6 mm in diameter was used. The pin tool rotational rates were from 600 to 1400 rpm, and the welding speeds were from 200 to 600 mm/min.

The specimens for microstructural examinations were cross sectioned perpendicular to the FSW direction. Microstructural characterization were carried out using scanning electron microscopy (SEM) (JEOL\*

\*JEOL is a trademark of Japan Electron Optics Ltd., Tokyo, Japan.

JSM-6380LV) coupled with energy dispersive X-ray spectroscopy (EDS) and three-dimensional (3-D) fractographic analysis capacity, X-ray diffractometry (XRD) (D/max 2500 PC), electron backscattered diffraction (EBSD, HKL), transmission electron microscopy (TEM) (FEI TECNAIG2), and high-resolution transmission electron microscopy (HRTEM). The specimens for EBSD were prepared by electrochemical polishing with 160 mL nitric acid + 640 mL methanol at  $-30^{\circ}\text{C}$ . The TEM thin foils, 3 mm in diameter, were prepared by twin-jet electropolishing using a solution of 70 pct methanol and 30 pct nitric at  $-35^{\circ}\text{C}$  and 19 V.

Vickers microhardness distribution maps were measured on the cross section perpendicular to the welding direction using a computerized Buehler hardness tester under a load of 300 g for 15 seconds. A total of seven test lines were measured through the cross section at an interval of 0.5 mm with a total of 567 indentations, as schematically shown in Figure 1. Subsize fatigue specimens referring to ASTM E8 standard, with a parallel

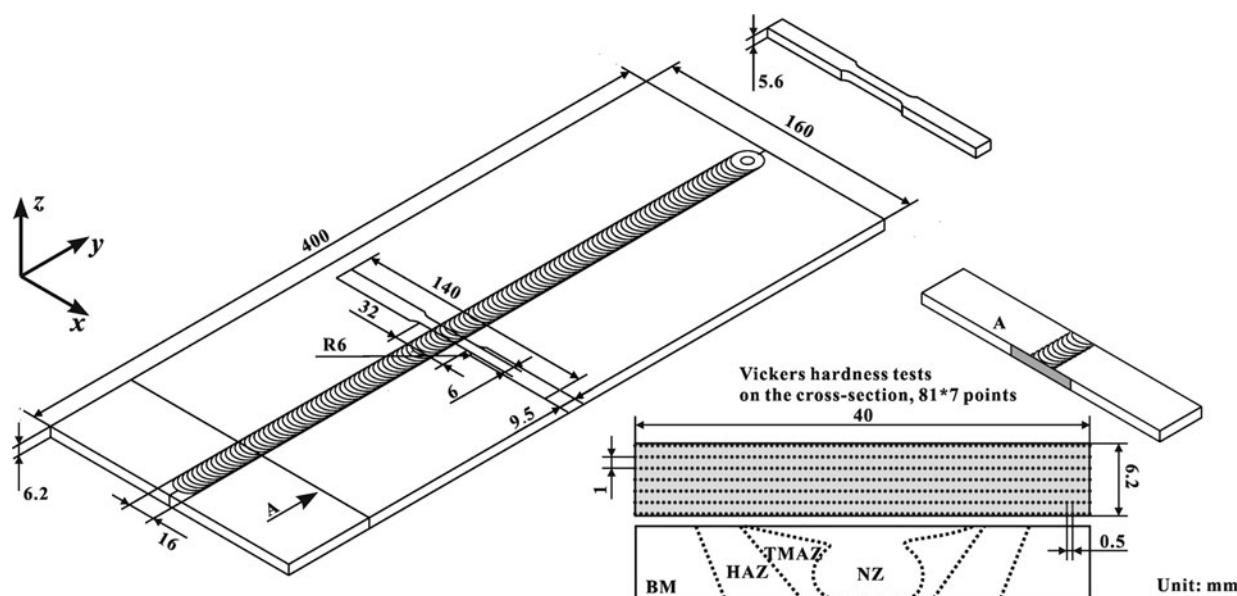


Fig. 1—Schematic illustration of friction-stir-welded 6061Al-T651 joints showing fatigue specimen machining, microindentation hardness test path, and various zones (BM, HAZ, TMAZ, and NZ) across the weld.<sup>[32]</sup>

section of  $32 \times 6 \times 5.6$  mm in size, were machined perpendicular to the FSW direction, as indicated in Figure 1. The fatigue specimens were ground with SiC papers up to grit 600 to remove the machining marks and to achieve a consistent and smooth surface. Total strain-controlled, push-pull type LCF tests were conducted using a computerized Instron fatigue testing system (Instron, Norwood, MA). The strain was measured using an extensometer with a gage length of 25 mm. In the fatigue testing, a triangular waveform with a strain ratio of  $R = -1$  was applied at a constant strain rate of  $1 \times 10^{-2} \text{ s}^{-1}$ . The strain-controlled testing at low total strain amplitudes was carried out until 10,000 cycles, after which it was changed to a load-control test at a frequency of 50 Hz. Total strain amplitudes of 0.2 to 0.8 pct were selected, where at least two specimens were tested at each level of strain amplitude. After the fatigue tests, the crack initiation sites and propagation mechanisms were examined *via* SEM.

### III. RESULTS

#### A. Microstructure

A typical orientation map of the 6061Al-T651 alloy is shown in Figure 2(a), where high-angle grain boundaries (HAGBs) with grain misorientations  $\geq 15$  deg are depicted by black lines. It is seen that 6061Al-T651 alloy consisted of large, elongated, pancake-shaped grains, a typical structure in a hot-rolled plate. The misorientation distribution of 6061Al-T651 alloy is different from a random grain assembly predicted by Mackenzie for randomly oriented cubes<sup>[37,38]</sup> (Figure 2(b)). Figure 2(c) shows a scanning transmission electron microscopy (STEM) image of a high density of fine needle-shaped precipitates and the coarse dispersoids as indicated by a white arrow, which consisted of aluminum, chromium, manganese, iron, and silicon, as revealed by the EDS spectrum inserted at the upper right corner on the image (Figure 2(c)). Figure 2(d) demonstrates the needle-shaped precipitates and the dislocations pinned by the coarse dispersoid. Figure 2(e) presents a STEM image of a high density of fine needle-shaped precipitates at a higher magnification. Figure 2(f) illustrates an HRTEM lattice image of the fine needle-shaped precipitates in the 6061Al-T651 alloy at a further higher magnification. As shown in Figure 3, the XRD pattern of the 6061Al-T651 alloy revealed the presence of Al,  $\text{Mg}_2\text{Si}$ ,  $\text{Mg}_5\text{Si}_6$ ,  $\text{Al}_7\text{Cu}_2\text{Fe}$ , and (Al,Fe,Si) phases.

After FSW, the nugget zone (NZ) of the friction-stir-welded 6061Al-T651 alloy (1400 rpm–600 mm/min) was characterized by fine and equiaxed recrystallized grain structure (Figure 4). However, the coarse dispersoids were still seen in the NZ (Figures 4(a) through (c)). The dispersoids were distributed both within the grain and at the grain boundary, as indicated by arrows in Figure 4(b). It is of interest to observe from Figure 4(b) that while the dislocation density in the NZ was quite low, some dislocations were pinned by the dispersoids. As seen from Figure 4(c), the STEM image indicated that a considerable amount of dispersoids was randomly

distributed both within grains and at grain boundaries. Like those existing in the unwelded base metal (BM) (Figure 2(c)), the dispersoids in the NZ contained aluminum, chromium, manganese, iron and silicon as well, as revealed by the EDS analysis shown in the insert of Figure 4(c). No other fine precipitates were observed any more *via* STEM examinations (Figure 4(c)).

As the welding speed decreased from 600 to 200 mm/min and the rotational rate from 1400 to 600 rpm, the NZ was still characterized by fine recrystallized grain structure (Figure 5(a)). However, more dislocations became piled up and pinned by the coarser dispersoids (Figure 5(b)). The thermomechanically affected zone (TMAZ) of friction-stir-welded joint (600 rpm–200 mm/min) was shown in Figures 5(c) and (d), where substructure and denser dislocation walls were clearly visible.

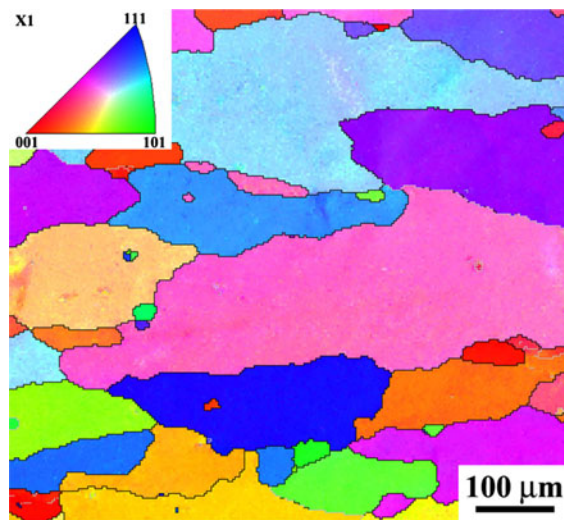
#### B. Microhardness

Figure 6 shows the microhardness contour maps for the friction-stir-welded 6061Al-T651 joints with different FSW parameters, which were plotted from 567 hardness values obtained across each welded joint following the pathway indicated in Figure 1. Two LHZs, located in the HAZ adjacent to the border between the TMAZ and HAZ, are obviously seen. The width of the LHZs increased and the hardness values of the LHZs decreased with decreasing welding speed from 600 to 200 mm/min while keeping a rotational rate constant of 1400 rpm (Figures 6(a) and (b)). However, the width and the hardness values of the LHZs were nearly independent of the rotational rate when it changed from 1400 to 1000 rpm (Figures 6(b) and (c)). The asymmetry of the weld was noticeable between the advancing side (AS) and retreating side (RS).

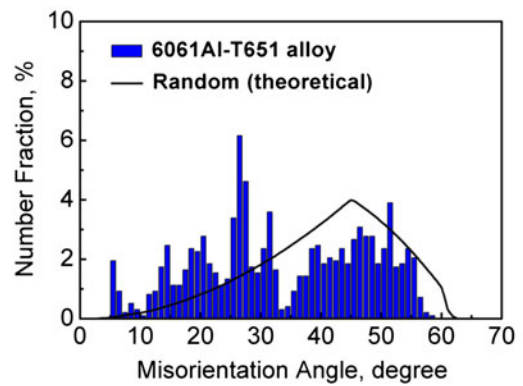
#### C. LCF Behavior

Figure 7 shows the variation of the stress amplitude and plastic strain amplitude with the number of cycles for the BM and friction-stir-welded joints made at a given rotational rate of 1400 rpm and different welding speeds, tested at total strain amplitudes from 0.4 to 0.8 pct. The following major features can be seen in Figure 7(a). First, the stress amplitude increased and fatigue life decreased with increasing total strain amplitude. Second, the stress amplitudes of the friction-stir-welded joints were lower than that of the BM. Third, the stress amplitudes increased with increasing welding speed. Fourth, the cyclic hardening characterized by the increase in the stress amplitude for the friction-stir-welded joints was much stronger than that for the BM. As cyclic deformation proceeded, the BM remained basically cyclic stable or displayed only slight cyclic hardening, while the friction-stir-welded joints exhibited significant cyclic hardening. These cyclic hardening characteristics could be correspondingly seen in Figure 7(b), where the variation of the plastic strain amplitude was expected to be just in contrast to that of the stress amplitude (Figure 7(a)). For instance, the stronger cyclic hardening of the welded joints, in

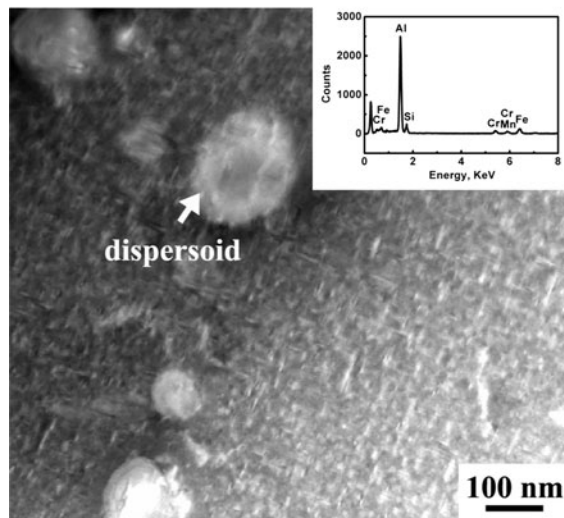




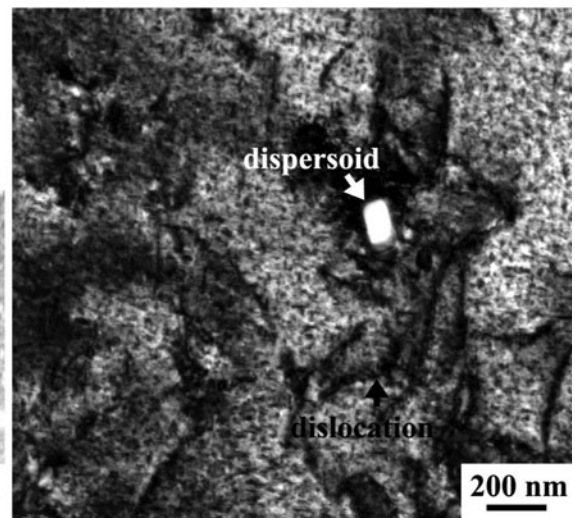
(a)



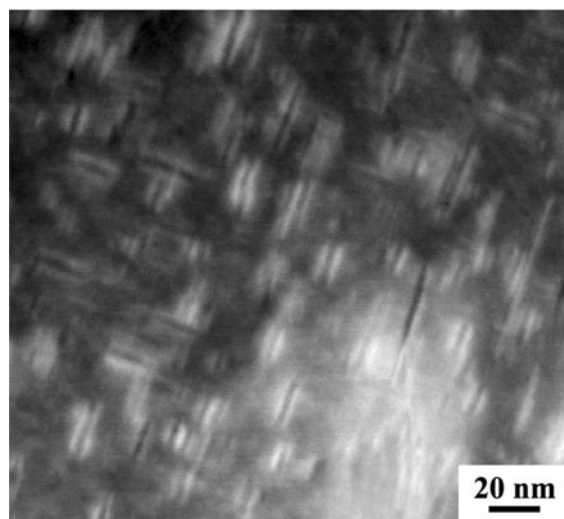
(b)



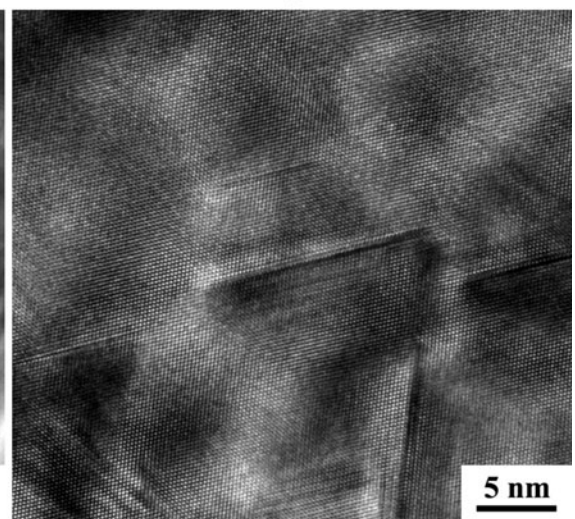
(c)



(d)



(e)



(f)

Fig. 2—Microstructure of 6061Al-T651 BM: (a) EBSD orientation map (the unit triangle legend), (b) number fractions vs misorientation angle, (c) STEM image showing the coarse dispersoids and the uniformly distributed tiny precipitates (inserted graph showing the EDS spectrum of the coarse dispersoid as indicated by a white arrow), (d) TEM image showing the tiny precipitates and the dislocations pinned by the coarse dispersoid, (e) STEM image showing the needlelike primary strengthening precipitates, and (f) HRTEM image showing the fine needlelike primary strengthening precipitates.

comparison with the BM, was represented by the more drastic decrease in the plastic strain amplitude. As well, the plastic strain amplitude of the BM was much lower

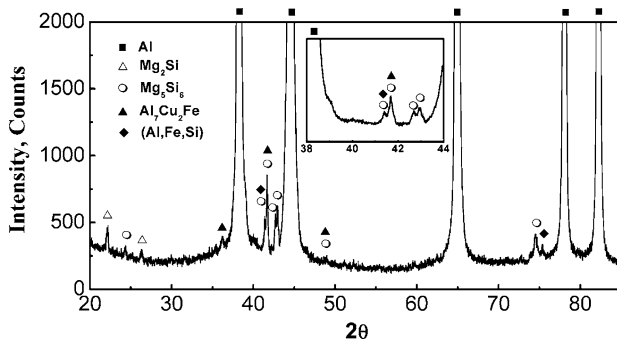


Fig. 3—XRD pattern of the 6061Al-T651 alloy.

than that of the welded joints at a given total strain amplitude applied. The changes in the cyclic deformation characteristics after FSW were directly associated with the microstructural changes and softness of the welded joints, as shown in Figures 4 through 6. For a given material, the occurrence of cyclic hardening-softening behavior was basically dependent on the initial state of the material provided that the test conditions were kept the same.<sup>[39]</sup> That is, the initially hardened material would be cyclically softened, while the initially softened material would be cyclically hardened. As a result, cyclic hardening would be anticipated for the initially softened friction-stir-welded joints (Figure 6).

Figure 8 shows the effect of the rotational rate from 600 to 1400 rpm on the cyclic hardening-softening behavior of the friction-stir-welded joints, in comparison with that of the BM. While a similar trend was observed, the effect of the rotational rate itself became

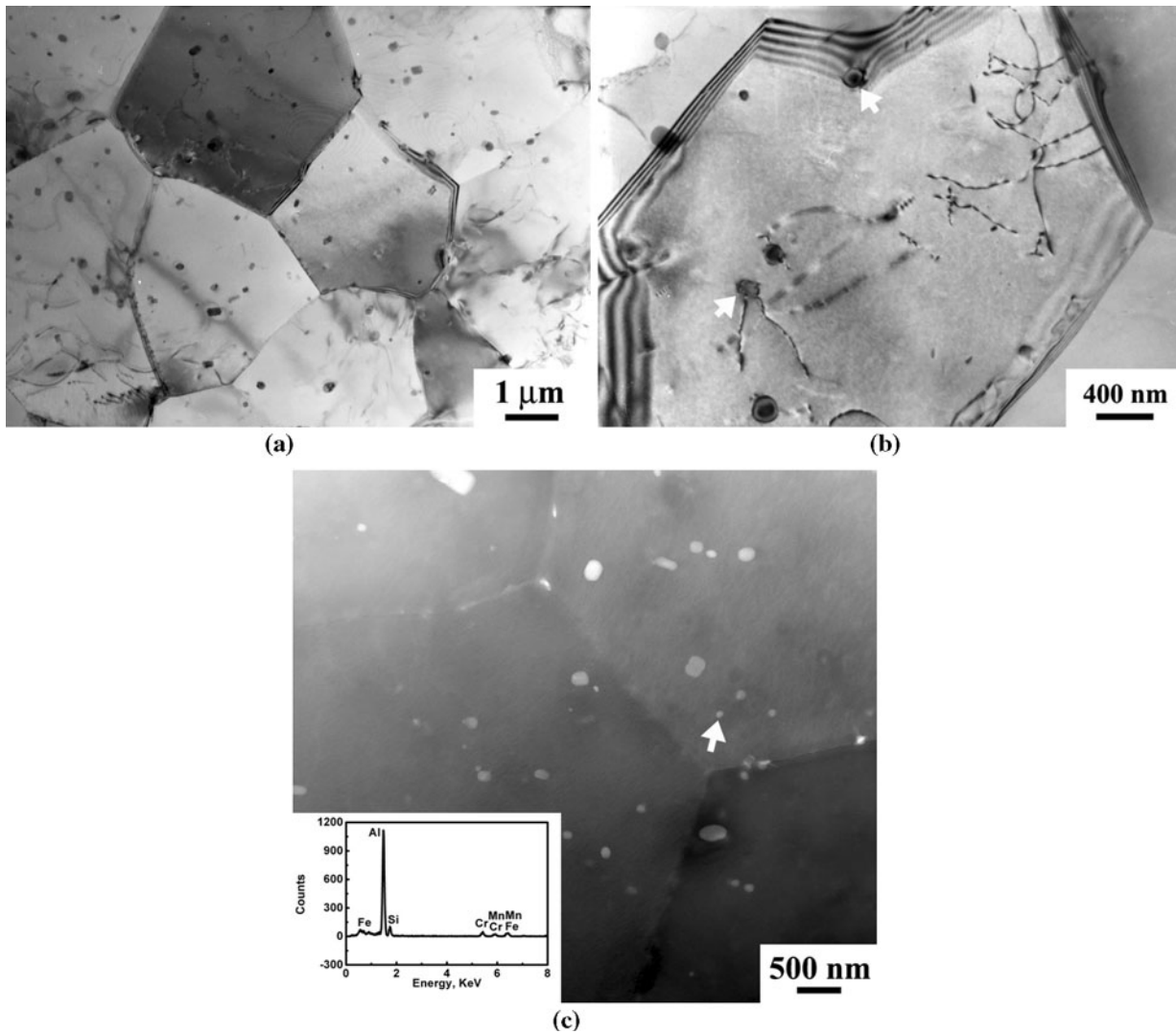


Fig. 4—TEM images of the NZ in the friction-stir-welded 6061Al-T651 alloy (1400 rpm–600 mm/min): (a) fine and equiaxed grains, (b) dispersoids as indicated by white arrows and dislocations pinned by the dispersoids, and (c) dispersoids in STEM image (inserted graph showing the EDS spectrum of the dispersoid as indicated by the white arrow).



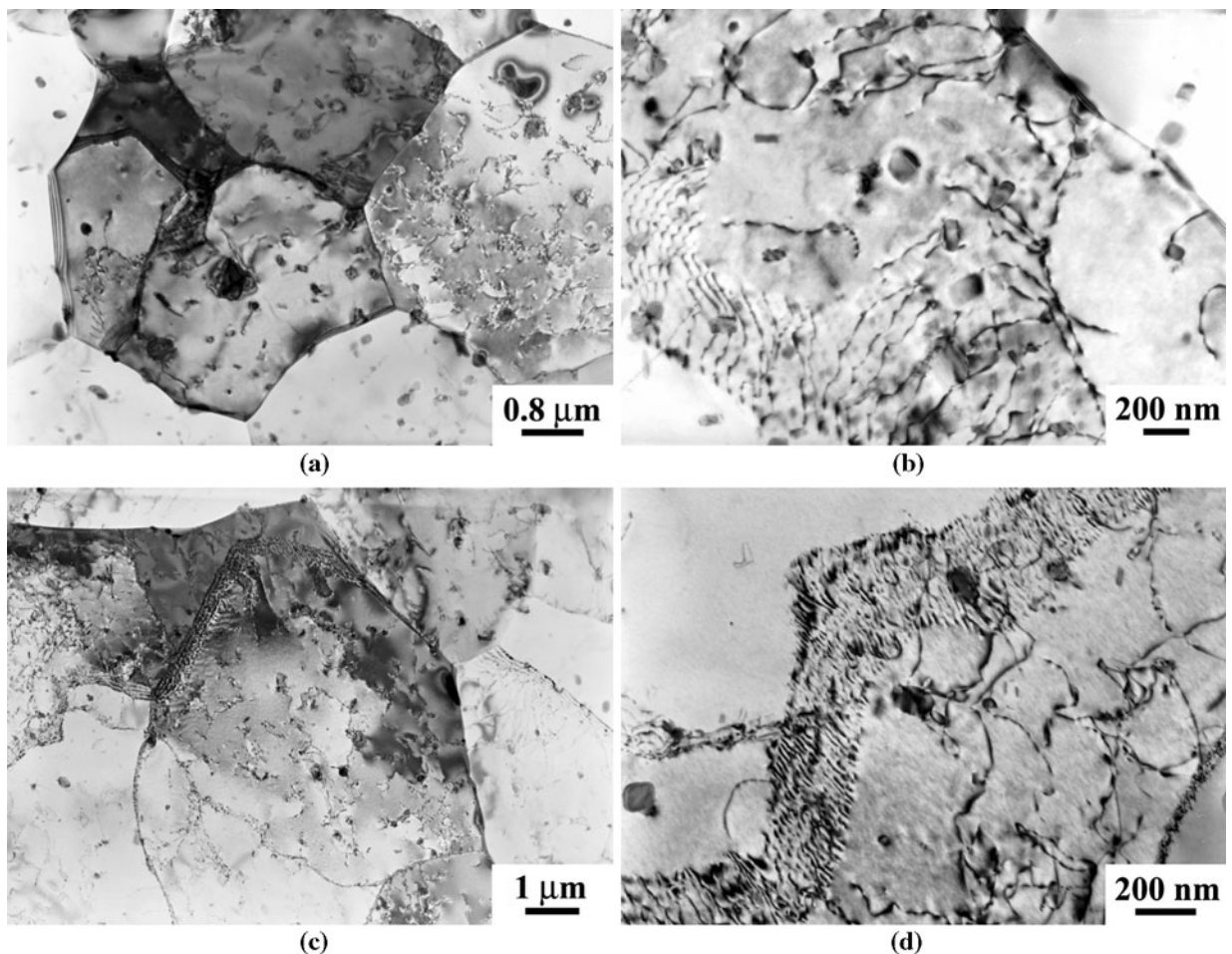


Fig. 5—TEM images of the friction-stir-welded 6061Al-T651 joint (600 rpm–200 mm/min): (a) and (b) NZ and (c) and (d) TMAZ, showing the subgrain structure and dislocations pileup.

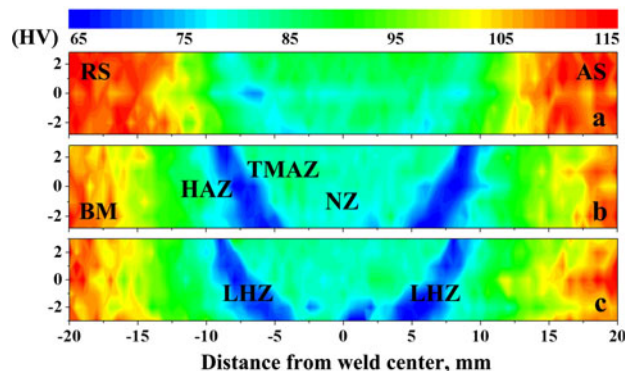


Fig. 6—Microhardness contour maps for the friction-stir-welded 6061Al-T651 joints: (a) 1400 rpm–600 mm/min, (b) 1400 rpm–200 mm/min, and (c) 1000 rpm–200 mm/min.

much smaller or negligible in view of the experimental scatter, as compared with that of the welding speed (Figure 7). This could be seen from the evolution of both the stress amplitude (Figure 8(a)) and the plastic strain amplitude (Figure 8(b)) as cyclic deformation progressed. Thus, the cyclic hardening of the friction-stir-welded joints was nearly independent of the rota-

tional rate at a given total strain amplitude. The total strain amplitude against the number of cycles to failure plotted on a semilog scale is shown in Figure 9. While the fatigue life of the friction-stir-welded joints was lower than that of the BM to a certain extent at higher strain amplitudes, the samples welded with the optimal parameters of 1400 rpm and 600 mm/min reached nearly the same fatigue life as that of the BM samples. It is also seen that at the low strain amplitude of 0.2 pct, the fatigue life presented in the semilog scale diagram appeared to be equivalent within the experimental scatter for both the BM and friction-stir-welded joints, regardless of the welding speed and pin tool rotational rate. This could be understood by the observations of the failure location in the following section.

#### D. Failure Location and Fractography

Figure 10 showed the failed LCF specimens. For the BM, some samples tended to fail at the end of the gage length at different total strain amplitudes due to the presence of potential stress concentration. The majority of friction-stir-welded joints failed along the LHZs and exhibited shear fracture mode. The shear fracture path

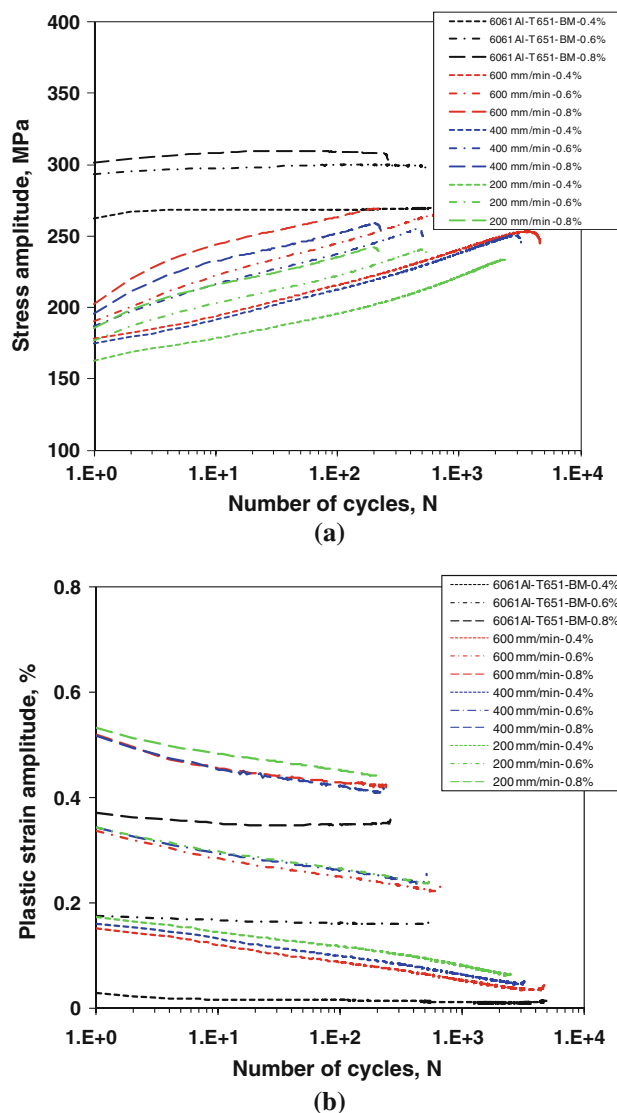


Fig. 7—(a) stress amplitude and (b) plastic strain amplitude vs the number of cycles at different total strain amplitudes for the 6061Al-T651 alloy welded with different welding speeds at a given rotational rate of 1400 rpm.

was oriented at an angle of about 45 to 60 deg to the tensile axis. At a lower total strain amplitude of 0.2 pct, the friction-stir-welded joints tended to fail at the end of the gage length, similar to the situation of BM. This seemed to suggest that at the low strain amplitude, there was no degradation or effect of the FSW on the fatigue resistance of 6061Al-T651 alloy. This could be well corroborated by the fatigue life data obtained at the strain amplitude of 0.2 pct in which the fatigue life was almost the same for both the BM and friction-stir-welded joints (Figure 9).

Figure 11 shows some typical fatigue fracture surfaces of a friction-stir-welded joint (1400 rpm–600 mm/min) tested at a total strain amplitude of 0.6 pct. The failure occurred in the LHZ or in the HAZ close to the border between the TMAZ and HAZ. It is seen that fatigue crack initiated from the specimen surface, as indicated by the dashed curve in Figure 11(a). The propagation

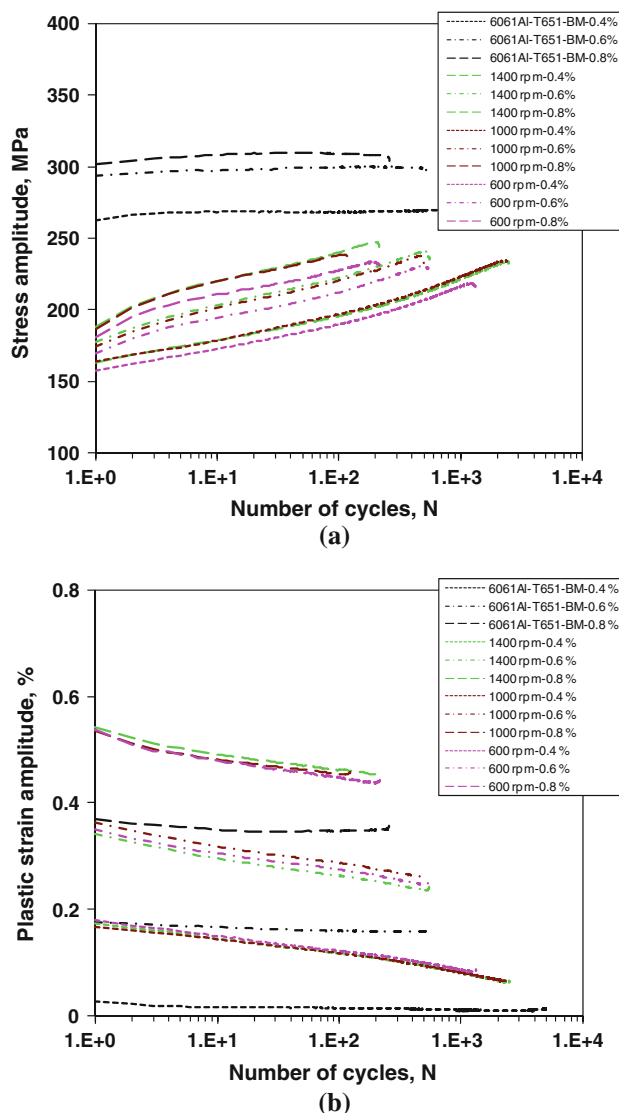


Fig. 8—(a) Stress amplitude and (b) plastic strain amplitude vs the number of cycles at different total strain amplitudes for the 6061Al-T651 alloy welded with different rotational rate at a given welding speed of 200 mm/min.

was basically characterized by characteristic fatigue striations (Figure 11(b)). Secondary cracks and white particles were observed at higher magnifications (Figure 11(c)). The white particles could be better seen from the backscattered electron image (Figure 11(d)). EDS analyses revealed that the white particles were iron and silicon containing particles (Figure 11(d)). Figure 11(e) shows a typical 3-D view of the propagation region in Figure 11(b). The steplike propagation was seen clearly in Figure 11(e).

Figure 12 shows some typical fatigue fracture surfaces of a friction-stir-welded joint (600 rpm–200 mm/min) tested at a total strain amplitude of 0.6 pct. Again, the failure location lay in the LHZ or in the HAZ adjoining to the border between the TMAZ and HAZ. It was seen that fatigue crack also initiated from the specimen surface (Figure 12(a)), and typical fatigue striations appeared in the propagation area (Figures 12(b) and



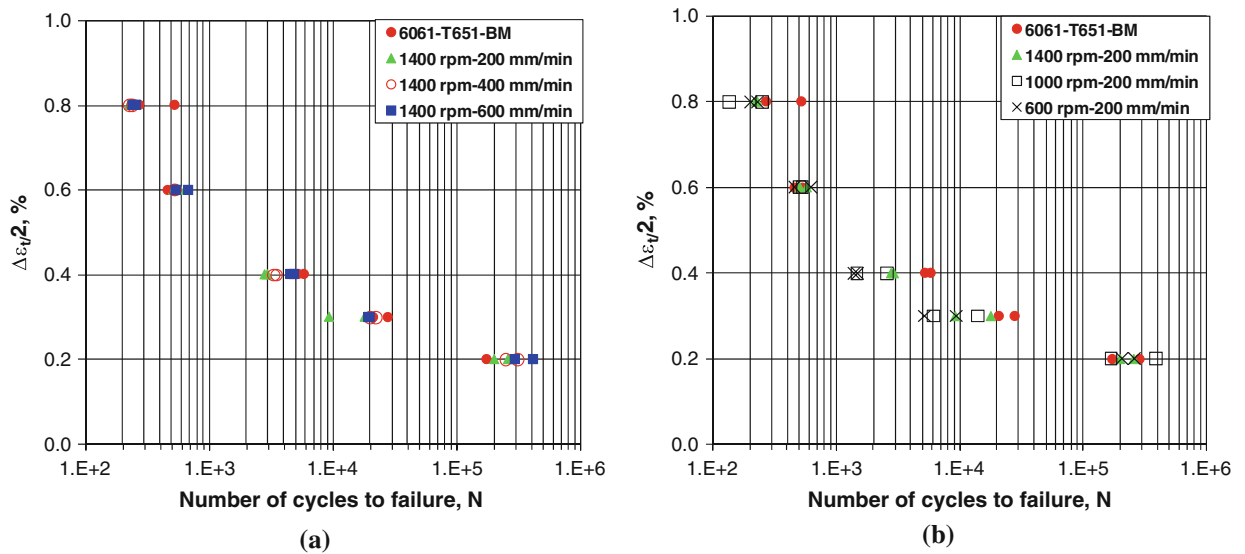


Fig. 9—Total strain amplitudes vs the number of cycles to failure for the BM and friction-stir-welded 6061Al-T651 joints welded at (a) different welding speeds (1400 rpm) and (b) different rotational rates (200 mm/min).

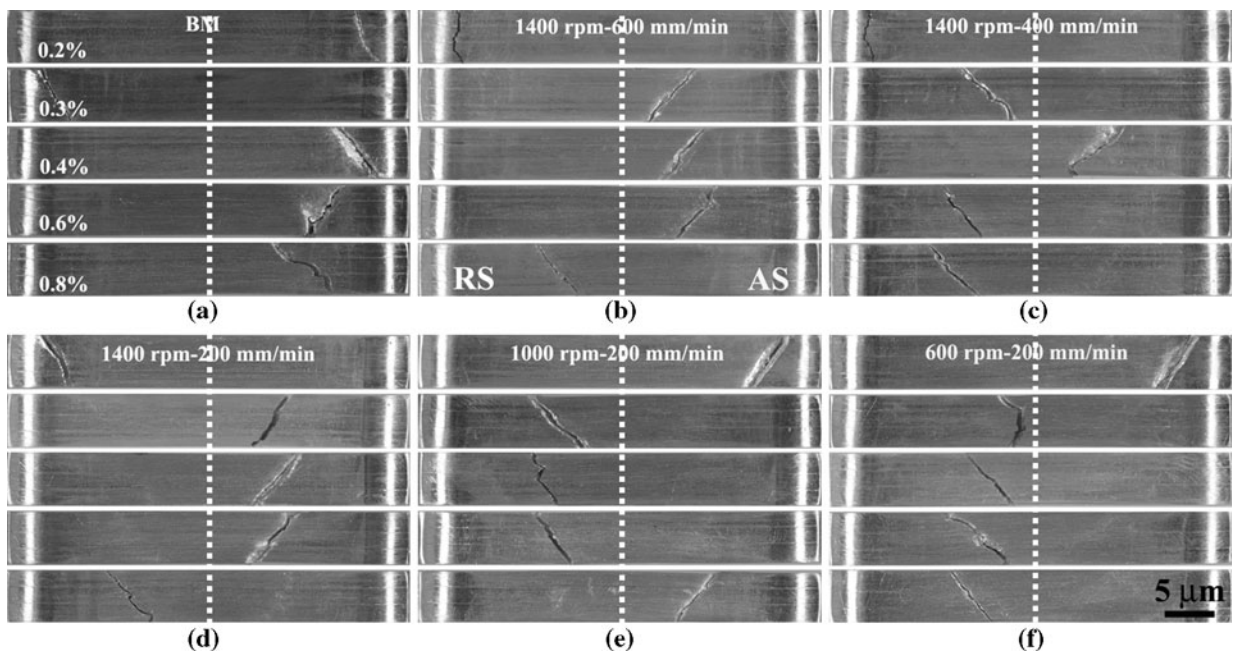


Fig. 10—Typical optical micrographs showing the failure locations of the 6061Al-T651 alloy fatigued at varying total strain amplitudes: (a) BM, (b) 1400 rpm-600 mm/min, (c) 1400 rpm-400 mm/min, (d) 1400 rpm-200 mm/min, (e) 1000 rpm-200 mm/min, and (f) 600 rpm-200 mm/min.

(c)), where some special patterns were observed. The magnified images showing the tiremark-like patterns indicated by two dashed boxes are shown in Figures 12(d) and (e). It is seen from Figure 12(d) that this tiremark pattern occurred between the fatigue striations. Figure 12(f) shows a 3-D view of the tiremark patterns corresponding Figure 12(e), where at the end (or top) of the right tiremark pattern, a cracked particle or inclusion of about  $5\ \mu\text{m}$  in length was clearly visible. The length of the inclusion corresponded well to the width of the right tiremark pattern in Figures 12(e) and (f). This provided direct evidence that the formation of the

tiremark patterns among the striations was a result of the interaction between the hard undissolved particles/inclusions pre-existent in the aluminum alloy and the relatively soft matrix in the LHZ under cyclic loading.

## IV. DISCUSSION

### A. Microstructural Characteristics

Dynamic recrystallization (DRX), which occurs during straining, has long been considered to be restricted to low stacking fault energy (SFE) metals. In high SFE

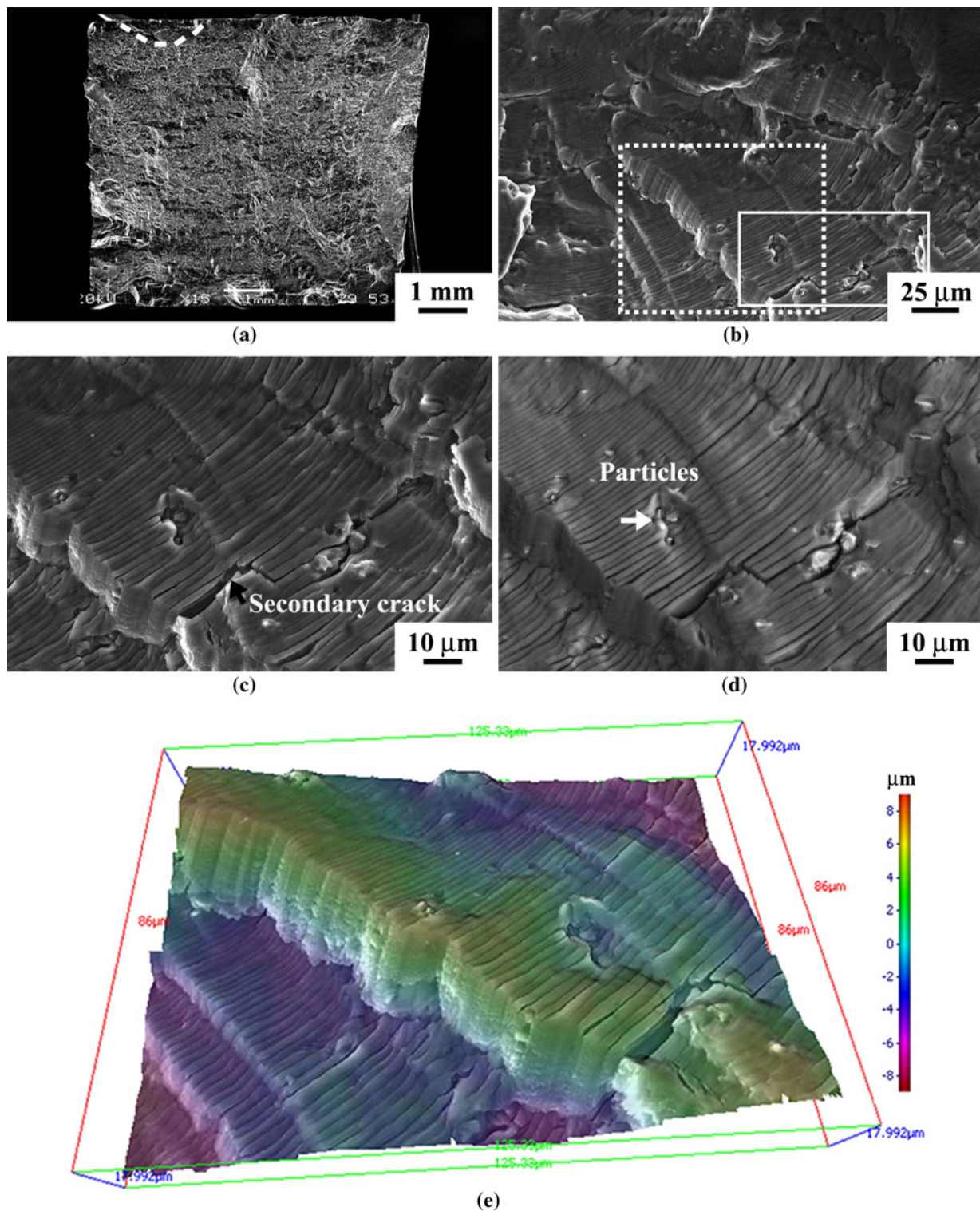


Fig. 11—Typical SEM micrographs of the friction-stir-welded 6061Al-T651 joint fatigued at a total strain amplitude of 0.6 pct (1400 rpm–600 mm/min): (a) overall view of the fracture surface, (b) a magnified view near the initiation site, (c) a magnified secondary electron image of the rectangular solid line box in (b), (d) a magnified backscattered electron image of the rectangular solid line box in (b), and (e) a 3-D image of the rectangular dashed line box in (b).

metals, *e.g.*, aluminum,<sup>[39]</sup> where the dislocation mobility was much larger, dynamic recovery (DRV) was assumed to be the only operating mechanism.<sup>[40]</sup> However, recent studies indicated the presence of fine

dynamically recrystallized grains possessing predominantly HAGBs and a low dislocation density in the friction-stir-welded aluminum alloys.<sup>[6,8,41]</sup> In the present study, the fine and equiaxed grains in the NZ of the



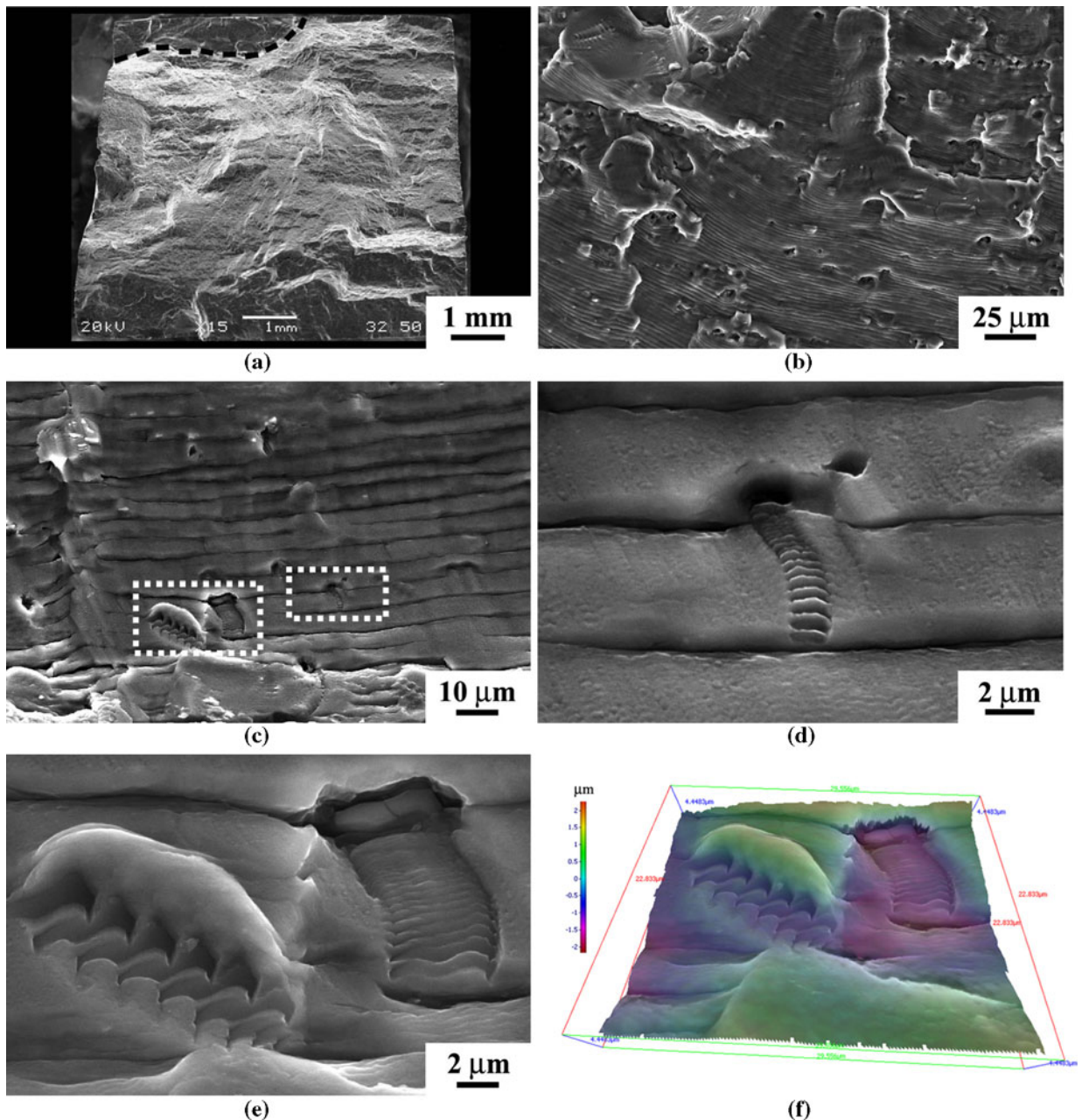


Fig. 12—Typical SEM micrographs of the friction-stir-welded 6061Al-T651 joint fatigued at a total strain amplitude of 0.6 pct (600 rpm–200 mm/min): (a) overall view of the fracture surface, (b) a magnified view near the initiation site, (c) fatigue striations at a higher magnification, (d) a further magnified view of the right dashed box in (c), (e) a further magnified view of the left dashed box in (c), and (f) a 3-D image corresponding to (e).

friction-stir-welded 6061Al-T651 alloy were achieved and they were considerably smaller than those in the BM. This indicated that DRX was a typical characteristic in the NZ of the friction-stir-welded 6061Al-T651 alloy (Figures 4 and 5). Fratini and Buffa<sup>[42]</sup> further reported a model on the continuous DRX in a friction-stir-welded AA6082-T6 aluminum alloy by a neural-network-based approach.

6xxx-series alloys with magnesium and silicon as the major alloying elements, often rendered precipitation strengthening.<sup>[43]</sup> Alloy elements such as silicon, manganese, iron, *etc.*, could have a significant influence on

the formation of intermetallic phases.<sup>[44–46]</sup> A large volume fraction of various coarse intermetallic particles (typically 1 pct) with sizes ranging between 1 and 10  $\mu\text{m}$ , depending on alloy chemical composition, were identified as  $\text{Al}_7\text{Cu}_2\text{Fe}$ ,  $\text{Al}_5\text{FeSi}$ ,  $\text{Al}_{12}(\text{Fe}, \text{Cr}, \text{Mn})_3\text{Si}$ , or stable  $\beta$  ( $\text{Mg}_2\text{Si}$ ) phase in 6xxx-series alloys.<sup>[47–50]</sup> Iron-bearing constituent phases typically found in 6xxx-series alloys included  $\beta$ - $\text{Al}_{12}\text{Fe}_3\text{Si}$  or  $\alpha$ - $\text{Al}_{12}\text{Fe}_3\text{Si}$ ; however, chromium or manganese could substitute for iron, and stabilized the formation of  $\alpha$ - $\text{Al}_{12}(\text{Fe}, \text{Cr}, \text{Mn})_3\text{Si}$ .<sup>[49]</sup> The presence of such a large number of intermetallic particles in different zones, especially in the LHZs where



the matrix became much softer (Figure 6), led to the formation of special tiremark patterns between the fatigue striations on the fracture surfaces under cyclic loading, as shown in Figure 12. Typically, chromium, manganese, and zinc were added to aluminum alloys to control recrystallization and grain structure.<sup>[51]</sup> The presence of grain refining element chromium resulted in the precipitation of  $\text{Al}_{12}\text{Mg}_2\text{Cr}$  dispersoids.<sup>[47,52]</sup>

In the heat-treatable aluminum alloys, improvements of the mechanical properties depended primarily on the nanosized precipitates, which acted as obstacles to the movement of dislocations *via* precipitation hardening.<sup>[4,53]</sup> The hardening effects (both the increase in the yield strength and the strain hardening rate) resulted from the interaction of dislocations with the nanosized precipitates.<sup>[53]</sup> In the interaction process, dislocations pinned by the precipitates under increasing applied stress would eventually either shear or bypass the precipitates (*i.e.*, Orowan strengthening mechanism). The obstacles for dislocation movement would be the precipitate itself and the strain connected with precipitates.<sup>[54]</sup> Although the precipitation processes in 6xxx-series alloys have been extensively studied, details of the precipitation sequence were alloy composition dependent (*i.e.*, the change of composition or the Mg:Si ratios) and have not yet been fully understood.<sup>[55,56]</sup> The small size of precipitates and the many possible variants of the orientation relation have made their structural evaluation difficult.<sup>[54]</sup> Compared with those in copper bearing 2xxx series alloy, the formation of metastable phases in 6xxx-series alloys required diffusion of both magnesium and silicon.<sup>[57,58]</sup> It was generally accepted that the precipitation sequence of the Al-Mg-Si alloys was as follows:<sup>[43,59]</sup> SSSS  $\rightarrow$  atomic clusters<sup>[60]</sup>  $\rightarrow$  initial  $\beta''$ <sup>[4,60]</sup>  $\rightarrow$  {pre- $\beta''$ <sup>[60,61]</sup>/needle-shaped  $\beta''$  precipitate<sup>[54,62,63]</sup>}  $\rightarrow$  {rod-shaped precipitates  $\beta'$ /lath-shaped  $B$  precipitates<sup>[3,64]</sup>/U1, U2<sup>[65]</sup>}  $\rightarrow$  { $\beta$ - $\text{Mg}_2\text{Si}$ <sup>[64,66]</sup>/Si<sup>[65]</sup>}, where SSSS represented the supersaturated solid solution. As shown in Figure 2(e) and (f), the fine needle-shaped  $\beta''$  primary strengthening precipitates were visible due to the strain field contrast.<sup>[67]</sup> Zandbergen *et al.*<sup>[54]</sup> reported that the composition and structure of the  $\beta''$  phase in an Al-Mg-Si alloy was determined to be  $\text{Mg}_5\text{Si}_6$ , which occurred as precipitates (typically 4 nanometers by 4 nanometers by 50 nanometers) and were associated with a particularly strong increase in the mechanical strength. As revealed by the XRD pattern shown in Figure 3, the  $\text{Mg}_5\text{Si}_6$  diffraction peaks were distinctly visible in the BM, indicating a high density precipitates ( $\beta''$ - $\text{Mg}_5\text{Si}_6$ ) presented in the BM, as shown in Figures 2(e) and (f). It should be noted that the precipitation process in aluminum alloys was diffusion controlled.<sup>[56]</sup> Aging always involved the diffusion of magnesium and silicon atoms in the aluminum. Dislocations were known to be sites for heterogeneous nucleation and paths for increased atomic transport during growth. However, the  $\text{Mg}_2\text{Si}$  phase was observed to nucleate at vacancy sites.<sup>[68]</sup>

After FSW, the NZ was characterized by fine and equiaxed recrystallized grain structure, and no fine  $\beta''$  precipitates were observed any more *via* TEM examinations, as shown in Figures 4 and 5. Thus, FSW resulted

in the dissolution of fine  $\beta''$  precipitates. It should be pointed out that the change in the precipitates was strongly influenced by the thermal hysteresis during FSW.<sup>[13]</sup> Previous DSC studies showed that the occurrence of  $\beta''$  and  $\beta'$  dissolution/precipitation produced a strong exothermic peak at  $\sim 250^\circ\text{C}$  and  $\sim 290^\circ\text{C}$ , respectively.<sup>[2,69,70]</sup> Therefore, the thermal cycle above  $250^\circ\text{C}$ , like the present FSW, would result in the dissolution of the needle-shaped precipitates in the Al-Mg-Si alloy, as shown in Figures 4 and 5.

## B. Microhardness

As shown in the hardness profile maps (Figure 6), two issues are worth discussion. First, two LHZs, located in the HAZ adjacent to the boundary between the TMAZ and HAZ, were obviously formed due to the dissolution of the needle-shaped  $\beta''$  primary strengthening precipitates existent in 6061Al-T651 base alloy, as discussed previously. The formation of the LHZs could also be attributed to the precipitate overaging,<sup>[35]</sup> crystallographic texture,<sup>[19]</sup> and grain/subgrain structure<sup>[71]</sup> depending on the peak temperature experienced. The LHZs, characterized by a low density of  $\beta'$  precipitates, experienced a peak temperature from about  $360^\circ\text{C}$  to  $370^\circ\text{C}$  with various durations.<sup>[35]</sup> Indeed, the highest temperature during FSW occurred at the top surface of the NZ.<sup>[6]</sup> While the high temperature in the NZ led to the dissolution of  $\beta''$  phase, the stronger solid solution strengthening and smaller grain size due to DRX during FSW (Figures 4 and 5) gave rise to a higher hardness in the NZ compared with the LHZs (Figure 6). Second, the location of LHZs changed and the width of the LHZs increased with decreasing welding speed from 600 to 200 mm/min (Figures 6(a) and (b)). However, the location and width of LHZs changed little with decreasing rotational rate from 1400 to 1000 rpm (Figures 6(b) and (c)). The asymmetry of the weld was noticeable between the AS and RS as well. A similar result has also been observed in a friction-stir-welded 2519Al-T87 alloy.<sup>[71]</sup> These changes were again related to the variation in the peak temperature experienced in the different zones as a function of the location or distance from the weld centerline, which in turn influenced the dissolution or coarsening of precipitates and the ensuing hardness profile (Figure 6). The increase of the LHZ width with decreasing welding speed was basically associated with a higher peak temperature and longer duration experienced by a wider area of the welded workpiece since the heat flow or transfer was a time-dependent process. Similar results on the effect of welding speed on the LHZ width were also reported by Lee *et al.*,<sup>[72]</sup> where the softened area was narrower at the higher welding speed than that at the lower welding speed.

## C. LCF Behavior

### 1. Cyclic hardening

It is seen from both Figures 7 and 8 that the FSW resulted in a much stronger cyclic hardening, while a decrease in the initial cyclic stress amplitude and an increase in the initial plastic strain amplitude occurred

after the FSW, regardless of the change in the welding speed (Figure 7) and rotational rate (Figure 8). At the higher total strain amplitude, the friction-stir-welded joints demonstrated a two-stage cyclic hardening characteristic, *i.e.*, the cyclic hardening appeared stronger within the initial three to four cycles; then the increase in the stress amplitude (Figures 7(a) and 8(a)) or decrease in the plastic strain amplitude (Figures 7(b) and 8(b)) became slower and almost linear until failure on the semilog scale as cyclic deformation proceeded. It is of particular interest to observe some similarities and differences of the cyclic hardening characteristics between the 6061Al-T651 alloy in the present study and the 7075Al-T651 alloy presented in Reference 32 after FSW. The similarities included that after the FSW, both alloys in the same temper condition (T651) displayed a lower initial stress amplitude and a higher initial plastic strain amplitude, cyclic hardening took place, and a two-stage character emerged. The major difference lay in the variation trend in the cyclic hardening behavior. Unlike the cyclic deformation evolution of the friction-stir-welded 6061Al-T651 alloy shown in Figures 7 and 8, the friction-stir-welded 7075Al-T651 alloy showed an initial slower cyclic hardening followed by a stronger and nearly linear cyclic hardening (also on the semilog scale) in the intermediate stage, and finally approached a steady-state cyclic hardening.<sup>[32]</sup> It is seen that in the friction-stir-welded 6061Al-T651 alloy (Figures 7 and 8), the two-stage cyclic hardening character appeared to occur only at higher total strain amplitudes, while it was more obvious with a wider range of total strain amplitudes applied in the case of friction-stir-welded 7075Al-T651 alloy.<sup>[32]</sup> Furthermore, it was observed that at the given total strain amplitude applied, the cyclic stress amplitude was lower and the plastic strain amplitude was higher in the friction-stir-welded 6061Al-T651 alloy than in the friction-stir-welded 7075Al-T651 alloy. This seemed to suggest that the undissolved  $E$  phase ( $Mg_3Cr_2Al_{18}$ ) present in the friction-stir-welded 7075Al-T651 alloy joints would be more effective in the cyclic strengthening/hardening than the undissolved complicated multiple intermetallic particles/inclusions

(*e.g.*,  $Al_7Cu_2Fe$ ,  $Al_5FeSi$ ,  $Al_{12}(Fe,Cr,Mn)_3Si$ ,  $Mg_2Si$ ,  $\beta-Al_9Fe_2Si_2$ ,  $\alpha-Al_{12}Fe_3Si$ ,  $\alpha-Al_{12}(Fe,Cr,Mn)_3Si$ , and  $Al_{12}Mg_2Cr$ ) in the friction-stir-welded 6061Al-T651 alloy joints. It was likely that the preceding particles/inclusions might have different degrees of obstruction to the movement of dislocations during cyclic (or even just monotonic/tensile) deformation. Further studies on the individual role of these intermetallic particles/inclusions in the deformation of the friction-stir-welded 6061Al-T651 alloy joints are needed. Finally, as mentioned earlier in Section III-C, the occurrence of the overall cyclic hardening of the 6061Al-T651 alloy after the FSW observed in Figures 7 and 8, in comparison with the BM, was mainly attributed to the softness across the friction-stir-welded joints (Figure 6) since a higher dislocation storage capacity and stronger interaction between the dislocations and various undissolved intermetallic particles/inclusions would be expected. Similar hardening behavior in a friction-stir-welded AZ31B-H24 magnesium alloy and the relevant discussion could be seen in References 73 and 74, where the FSW also resulted in a softer welded joint and stronger strain hardening.

## 2. Monotonic and cyclic stress-strain curves

Figure 13 shows the cyclic stress-strain curves of the BM and friction-stir-welded 6061Al-T651 joints, in comparison with the corresponding monotonic stress-strain curves determined at the same strain rate of  $1 \times 10^{-2} \text{ s}^{-1}$ , where the cyclic stress-strain curve was obtained by connecting the tips of stable or midlife hysteresis loops from the constant strain amplitude fatigue tests of specimens cycled at different strain amplitudes.<sup>[39]</sup> The cyclic stress-strain curve could be described by the following equation:

$$\frac{\Delta\sigma}{2} = K' \left( \frac{\Delta\epsilon_p}{2} \right)^{n'} \quad [1]$$

where  $K'$  is the cyclic strength coefficient and  $n'$  is the cyclic strain hardening exponent. The evaluated  $K'$  and  $n'$  values according to Eq. [1] are given in Table I. It is

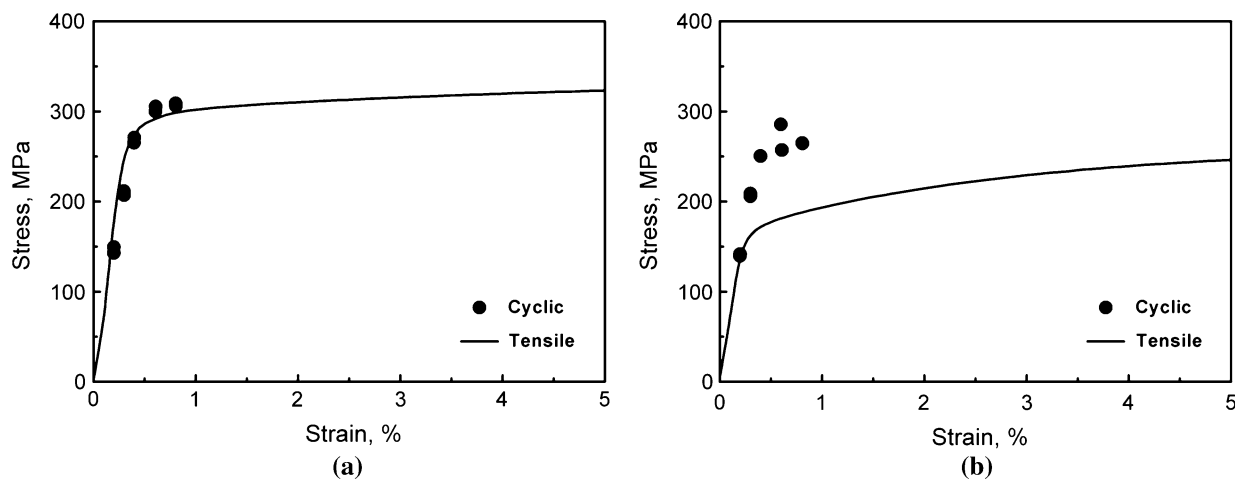


Fig. 13—Comparison between the monotonic and cyclic stress-strain curves obtained at a strain rate of  $1 \times 10^{-2} \text{ s}^{-1}$  for (a) BM and (b) friction-stir-welded joint (1400 rpm–600 mm/min).

seen that the cyclic strain hardening exponent, cyclic strength coefficient, and cyclic yield strength all increased with increasing welding speed from 200 to 600 mm/min. Again, the effect of the rotational rate between 600 and 1400 rpm on these parameters was relatively small while keeping the welding speed constant at 200 mm/min. In comparison with the BM, the friction-stir-welded 6061Al-T651 joint made with a welding speed of 600 mm/min and rotational rate of 1400 rpm exhibited only an approximate 10 pct drop in the cyclic yield strength and cyclic strain hardening exponent, and about 18 pct reduction in the cyclic strength coefficient. It is seen from Figure 13 that the cyclic strain hardening was stronger than the monotonic strain hardening in both BM and friction-stir-welded joints. However, the cyclic strain hardening after FSW became much more pronounced, as seen from Figure 13(b). This corresponded well to the cyclic hardening characteristics shown in Figures 7 and 8.

### 3. Fatigue life and LCF parameters

The total strain amplitude could be expressed as elastic strain amplitude ( $\Delta\epsilon_e/2$ ) and plastic strain amplitude ( $\Delta\epsilon_p/2$ ); i.e.,

$$\left(\frac{\Delta\epsilon_t}{2}\right) = \left(\frac{\Delta\epsilon_e}{2}\right) + \left(\frac{\Delta\epsilon_p}{2}\right) \quad [2]$$

The first part could further be expressed in terms of Basquin equation,

$$\frac{\Delta\epsilon_e}{2} = \frac{\sigma'_f(2N_f)^b}{E} \quad [3]$$

and the second term of Eq. [2] could be replaced by the Coffin-Manson relation,

$$\frac{\Delta\epsilon_p}{2} = \epsilon'_f(2N_f)^c \quad [4]$$

then,

$$\frac{\Delta\epsilon_t}{2} = \frac{\sigma'_f(2N_f)^b}{E} + \epsilon'_f(2N_f)^c \quad [5]$$

where  $E$  is the Young's modulus,  $N_f$  is the fatigue life or the number of cycles to failure,  $\sigma'_f$  is the fatigue strength coefficient,  $b$  is fatigue strength exponent,  $\epsilon'_f$  is the fatigue ductility coefficient, and  $c$  is the fatigue ductility exponent. The obtained experimental results indicated

that fatigue deformation followed the Coffin–Manson and Basquin's equations well, and the fatigue parameters evaluated on the basis of Eqs. [3] and [4] are summarized in Table I. Akin to the cyclic yield strength, cyclic strain hardening exponent, and cyclic strength coefficient, the fatigue strength coefficient of the friction-stir-welded joints also increased with increasing welding speed. The absolute value of the fatigue strength exponent of the friction-stir-welded joints also slightly increased, while the fatigue ductility coefficient and fatigue ductility exponent (absolute value) decreased as the welding speed increased from 200 to 600 mm/min. Like the cyclic hardening characteristics shown in Figures 7 and 8, no strong effect of the rotational rate on the fatigue parameters could be seen.

### 4. Smith, Watson, and Topper equation

Based on the Smith, Watson, and Topper (SWT) equation,<sup>[75]</sup>

$$\sigma_{\max}\epsilon_a = \frac{(\sigma'_f)^2}{E}(2N_f)^{2b} + \sigma'_f\epsilon'_f(2N_f)^{b+c} \quad [6]$$

where  $\sigma_{\max}$  is the maximum stress at the saturation or midlife and  $\epsilon_a$  is the strain amplitude ( $\Delta\epsilon/2$ ). Both the experimental data in the form of  $\sigma_{\max}\epsilon_a$  and Eq. [6] are plotted in Figure 14. It is seen that the obtained fatigue life followed the SWT equation well.

### D. Fractography

The fatigue process can be divided into three stages: crack initiation, crack propagation, and final fast fracture. Fatigue cracks often initiated at the surface or at voids or second-phase inclusions that served as stress risers.<sup>[76]</sup>

In this study, fatigue cracks initiated from the specimen surface in the LHZ in the friction-stir-welded samples (Figures 11(a) and 12(a)). Fatigue failure of friction-stir-welded joints was also found to initiate at surface roughness or flash on the surface of the joint, as well as typical FSW defects.<sup>[77]</sup> Fatigue crack propagation was basically characterized by the characteristic fatigue striations, together with some secondary cracks, observed at higher magnifications (Figures 11 and 12). The fatigue striations usually occurred by a repeated plastic blunting-sharpening process due to the slip of dislocations in the plastic zone at the fatigue crack

**Table I. LCF Parameters of 6061Al-T651 Alloy in Different Conditions**

FSW Parameters (rpm–mm/min)	Cyclic Yield Strength, $\sigma_{ys,c}$ (MPa)	Cyclic Strain Hardening Exponent, $n'$	Cyclic Strength Coefficient, $K'$ (MPa)	Fatigue Strength Coefficient, $\sigma'_f$ (MPa)	Fatigue Strength Exponent, $b$	Fatigue Ductility Coefficient, $\epsilon'_f$ (Pct)	Fatigue Ductility Exponent, $c$
6061Al-T651-BM	305	0.12	632	760	−0.12	0.22	−0.72
1400–600	275	0.11	520	509	−0.09	0.29	−0.71
1400–400	250	0.10	471	476	−0.09	0.34	−0.73
1400–200	232	0.09	408	436	−0.08	0.56	−0.79
1000–200	230	0.09	409	419	−0.08	0.24	−0.69
600–200	220	0.08	371	404	−0.08	0.41	−0.75



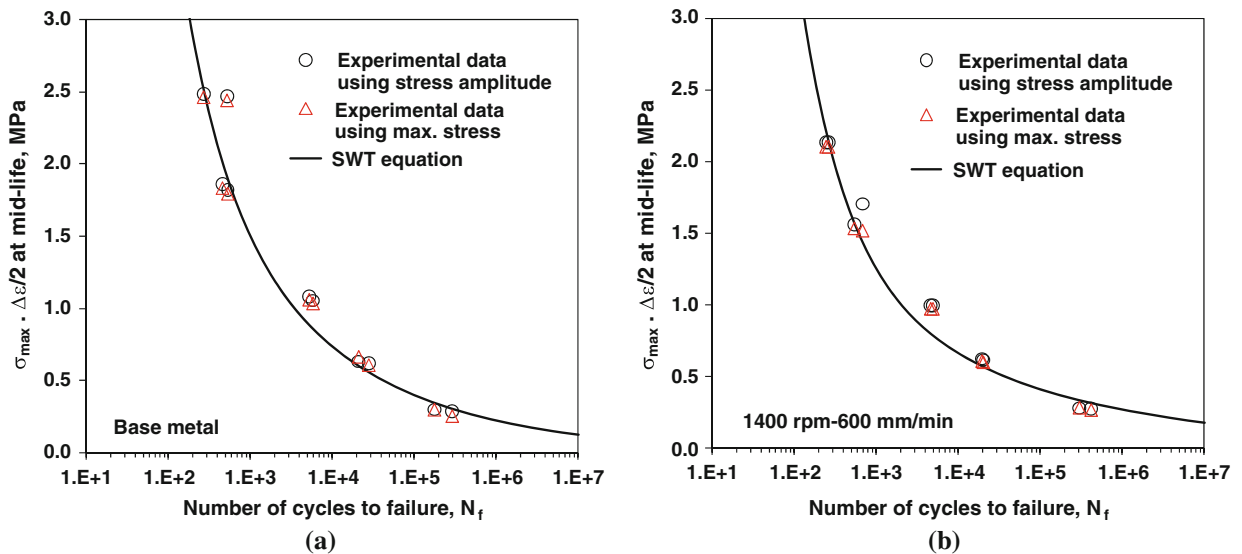


Fig. 14—Product of the maximum stress with the strain amplitude as a function of the number of cycles to failure for (a) BM and (b) friction-stir-welded joint (1400 rpm–600 mm/min).

tip.<sup>[78]</sup> As mentioned earlier, the observed tiremark patterns lying in-between the striations (Figures 12(c) through (f)) were attributed to the interaction between the undissolved hard particles/inclusions pre-existing in the aluminum alloy and the relatively soft matrix in the LHZ under cyclic loading. More detailed studies on the formation mechanism of the tiremark patterns are needed.

## V. CONCLUSIONS

1. The BM consisted of large, elongated, pancake-shaped grains with a high density of fine needle-shaped  $\beta''$  primary strengthening precipitates and coarse dispersoids. After FSW, the NZ was characterized by fine and equiaxed recrystallized grains and uniformly distributed coarse dispersoids, but the primary strengthening precipitates dissolved.
2. Two LHZs were observed to occur in the HAZ adjacent to the border between the TMAZ and HAZ, and their width decreased with increasing welding speed from 200 to 600 mm/min in the friction-stir-welded 6061Al-T651 alloy. No obvious effect of the rotational rate on the width of LHZs was observed.
3. While the FSW resulted in a lower stress amplitude, a higher plastic strain amplitude, and a lower fatigue life at a given total strain amplitude, the cyclic hardening of the friction-stir-welded joints became significantly stronger than that of BM. At higher total strain amplitudes, the friction-stir-welded joints exhibited a two-stage cyclic hardening characteristic, where the cyclic hardening was stronger within the initial few cycles and then became slightly weaker and almost linear on the semilog scale as cyclic deformation proceeded until failure.

4. The fatigue lifetime and cyclic stress amplitude increased and plastic strain amplitude slightly decreased with increasing welding speed from 200 to 600 mm/min, but they were nearly independent of the rotational rate between 600 and 1400 rpm. With increasing welding speed, the cyclic yield strength, cyclic strain hardening exponent, cyclic strength coefficient, and fatigue strength coefficient of the friction-stir-welded joints increased, while the fatigue ductility coefficient and fatigue ductility exponent (absolute value) decreased.
5. On a macroscopic view, the majority of the friction-stir-welded joints failed along the LHZs and exhibited a shear fracture mode with an angle at about 45 to 60 deg to the loading axis especially at higher strain amplitudes.
6. Fatigue crack initiation was observed to occur at the specimen surface or near-surface welding defect in the friction-stir-welded joints and crack propagation was characterized by the characteristic fatigue striations together with some secondary cracks. Some special tiremark patterns were observed to be present in-between the fatigue striations, which formed due to the interaction between the undissolved hard dispersoids/inclusions pre-existent in the 6061Al-T651 alloy and the relatively soft matrix in the LHZ under cyclic loading.

## ACKNOWLEDGMENTS

The authors thank the Natural Sciences and Engineering Research Council of Canada (NSERC) (Ottawa, ON, Canada), Premier's Research Excellence Award (PREA) (Toronto, ON, Canada), Canada Foundation for Innovation (CFI) (Ottawa, ON, Canada), Ryerson Research Chair (RRC) program of Ryerson University (Toronto, ON, Canada), National

Outstanding Young Scientist Foundation (Grant No. 50525103), National Natural Science Foundation of China (Beijing, China), and Hundred Talents Program of Chinese Academy of Sciences (Beijing, China) for providing financial support for this collaborative project. The authors also thank Messrs. Q. Li, A. Machin, J. Amankrah, D. Ostrom, and R. Churaman (Ryerson University, Toronto, ON, Canada) for their assistance in the experiments.

## REFERENCES

1. L.P. Troeger and E.A. Starke, Jr.: *Mater. Sci. Eng. A*, 2000, vol. 277A, pp. 102–13.
2. J.Y. Yao, D.A. Graham, B. Rinderer, and M.J. Couper: *Micron*, 2001, vol. 32, pp. 865–70.
3. M.A.V. Huis, J.H. Chen, H.W. Zandbergen, and M.H.F. Sluiter: *Acta Mater.*, 2006, vol. 54, pp. 2945–55.
4. J.H. Chen, E. Costan, M.A.V. Huis, Q. Xu, and H.W. Zandbergen: *Science*, 2006, vol. 312, pp. 416–19.
5. W.M. Thomas, E.D. Nicholas, J.C. Needham, M.G. Murch, P. Templesmith, and C.J. Dawes: G.B. Patent Application No. 9125978.8, Dec. 1991.
6. R.S. Mishra and Z.Y. Ma: *Mater. Sci. Eng. R*, 2005, vol. 50R, pp. 1–78.
7. R. Nandan, T. DebRoy, and H.K.D.H. Bhadeshia: *Prog. Mater. Sci.*, 2008, vol. 53, pp. 980–1023.
8. P.L. Threadgill, A.J. Leonard, H.R. Shercliff, and P.J. Withers: *Int. Mater. Rev.*, 2009, vol. 54, pp. 49–93.
9. B. Heinz and B. Skrotzki: *Metall. Mater. Trans. B*, 2002, vol. 33B, pp. 489–98.
10. A. Simar, Y. Brechet, B.D. Meester, A. Denquin, and T. Pardoen: *Acta Mater.*, 2007, vol. 55, pp. 6133–43.
11. C. Gallais, A. Denquin, Y. Brechet, and G. Lapasset: *Mater. Sci. Eng. A*, 2008, vol. 496A, pp. 77–89.
12. W. Woo, H. Choo, D.W. Brown, and Z.L. Feng: *Metall. Mater. Trans. A*, 2007, vol. 38A, pp. 69–76.
13. Y.S. Sato, H. Kokawa, M. Enomoto, and S. Jogan: *Metall. Mater. Trans. A*, 1999, vol. 30A, pp. 2429–37.
14. W. Woo, L. Balogh, T. Ungar, H. Choo, and Z.L. Feng: *Mater. Sci. Eng. A*, 2008, vol. 498A, pp. 308–13.
15. Y.S. Sato, H. Kokawa, K. Ikeda, M. Enomoto, S. Jogan, and T. Hashimoto: *Metall. Mater. Trans. A*, 2001, vol. 32A, pp. 941–48.
16. D.P. Field, T.W. Nelson, Y. Hovanski, and K.V. Jata: *Metall. Mater. Trans. A*, 2001, vol. 32A, pp. 2869–77.
17. W. Woo, H. Choo, D.W. Brown, S.C. Vogel, P.K. Liaw, and Z. Feng: *Acta Mater.*, 2006, vol. 54, pp. 3871–82.
18. S.W. Xu and X.M. Deng: *Acta Mater.*, 2008, vol. 56, pp. 1326–41.
19. Y.S. Sato and H. Kokawa: *Metall. Mater. Trans. A*, 2001, vol. 32A, pp. 3023–31.
20. S. Lim, S. Kim, C.G. Lee, and S. Kim: *Metall. Mater. Trans. A*, 2004, vol. 35A, pp. 2829–35.
21. M. Cabibbo, H.J. McQueen, E. Evangelista, S. Spigarelli, M.D. Paola, and A. Falchero: *Mater. Sci. Eng. A*, 2007, vols. 460–461A, pp. 86–94.
22. M. Ericsson and R. Sandstrom: *Int. J. Fatigue*, 2003, vol. 25, pp. 1379–87.
23. M.N. James, D.J. Hughes, D.G. Hattingh, G.R. Bradley, G. Mills, and P.J. Webster: *Fatigue Fract. Eng. Mater. Struct.*, 2004, vol. 27, pp. 187–202.
24. P.S. De, R.S. Mishra, and C.B. Smith: *Scripta Mater.*, 2009, vol. 60, pp. 500–03.
25. M.N. James, D.G. Hattingh, and G.R. Bradley: *Int. J. Fatigue*, 2003, vol. 25, pp. 1389–98.
26. K.V. Jata, K.K. Sankaran, and J.J. Ruschau: *Metall. Mater. Trans. A*, 2000, vol. 31A, pp. 2181–92.
27. P.S. Pao, S.J. Gill, C.R. Feng, and K.K. Sankaran: *Scripta Mater.*, 2001, vol. 45, pp. 605–12.
28. R. John, K.V. Jata, and K. Sadananda: *Int. J. Fatigue*, 2003, vol. 25, pp. 939–48.
29. M. Czechowski: *J. Mater. Proc. Technol.*, 2005, vols. 164–165, pp. 1001–06.
30. L. Ceschini, I. Boromei, G. Minak, A. Morri, and F. Tarterini: *Compos. A*, 2007, vol. 38, pp. 1200–10.
31. L. Ceschini, I. Boromei, G. Minak, A. Morri, and F. Tarterini: *Compos. Sci. Technol.*, 2007, vol. 67, pp. 605–15.
32. A.H. Feng, D.L. Chen, and Z.Y. Ma: *Metall. Mater. Trans. A*, 2010, vol. 41A, pp. 957–71.
33. M.W. Mahoney, C.G. Rhodes, J.G. Flintoff, R.A. Spurling, and W.H. Bingel: *Metall. Mater. Trans. A*, 1998, vol. 29A, pp. 1955–64.
34. Y.S. Sato, H. Kokawa, M. Enomoto, S. Jogan, and T. Hashimoto: *Metall. Mater. Trans. A*, 1999, vol. 30A, pp. 3125–30.
35. F.C. Liu and Z.Y. Ma: *Metall. Mater. Trans. A*, 2008, vol. 39A, pp. 2378–88.
36. A.H. Feng, D.L. Chen, and Z.Y. Ma: *Mater. Sci. Forum*, 2009, vols. 618–619, pp. 41–44.
37. J.K. Mackenzie: *Biometrika*, 1957, vol. 44, pp. 205–10.
38. J.K. Mackenzie: *Biometrika*, 1958, vol. 45, pp. 229–40.
39. G.E. Dieter: *Mechanical Metallurgy*, 3rd ed., McGraw-Hill, Boston, MA, 1986.
40. F. Montheillet, J. Lepinoux, D. Weygand, and E. Rauch: *Adv. Eng. Mater.*, 2001, vol. 3, pp. 587–89.
41. J.Q. Su, T.W. Nelson, R. Mishra, and M. Mahoney: *Acta Mater.*, 2003, vol. 51, pp. 713–29.
42. L. Fratini and G. Buffa: *J. Eng. Manufact.*, 2007, vol. 221, pp. 857–64.
43. C. Ravi and C. Wolverton: *Acta Mater.*, 2004, vol. 52, pp. 4213–27.
44. H. Tanihata, T. Sugawara, K. Matsuda, and S. Ikeno: *J. Mater. Sci.*, 1999, vol. 34, pp. 1205–10.
45. A.L. Dons, E.K. Jensen, Y. Langsrud, E. Tromborg, and S. Brusethaug: *Metall. Mater. Trans. A*, 1999, vol. 30A, pp. 2135–46.
46. G. Sha, K. O'Reilly, B. Cantor, R. Hamerton, and J. Worth: *Mater. Sci. Forum*, 2000, vols. 331–337, pp. 253–58.
47. T.S. Srivatsan, M.A. Hajri, M. Petraroli, B. Hotton, and P.C. Lam: *Mater. Sci. Eng. A*, 2002, vol. 325A, pp. 202–14.
48. C.A.W. Olea, L. Roldo, J.F.D. Santos, and T.R. Strohaecker: *Mater. Sci. Eng. A*, 2007, vols. 454–455, pp. 52–62.
49. J.E. Hatch: *Aluminum Properties and Physical Metallurgy*, ASM, Metals Park, OH, 1984.
50. D. Lassance, D. Fabregue, F. Delannay, and T. Pardoen: *Prog. Mater. Sci.*, 2007, vol. 52, pp. 62–129.
51. K. Laue and H. Stenger: *Extrusion: Process Machinery Tooling*, ASM INTERNATIONAL, Metals Park, OH, 1976.
52. E.A. Starke, Jr.: *Mater. Sci. Eng. A*, 1977, vol. 29A, pp. 99–115.
53. P. Donnadieu, G.F. Dirras, and J. Douin: *Mater. Sci. Forum*, 2002, vols. 396–402, pp. 1019–24.
54. H.W. Zandbergen, S.J. Andersen, and J. Jansen: *Science*, 1997, vol. 277, pp. 1221–25.
55. X. Wang, S. Esmaeili, and D.J. Lloyd: *Metall. Mater. Trans. A*, 2006, vol. 37A, pp. 2691–99.
56. R.S. Yassar, D.P. Field, and A. Weiland: *Metall. Mater. Trans. A*, 2005, vol. 36A, pp. 2059–65.
57. S.P. Chen, K.M. Mussert, and S.V.D Zwaag: *J. Mater. Sci.*, 1998, vol. 33, pp. 4477–83.
58. S.J. Andersen, C.D. Marioara, A. Froseth, R. Vissers, and H.W. Zandbergen: *Mater. Sci. Eng. A*, 2005, vol. 390A, pp. 127–38.
59. D.J. Chakrabarti and D.E. Laughlin: *Prog. Mater. Sci.*, 2004, vol. 49, pp. 389–410.
60. M.A.V. Huis, J.H. Chen, M.H.F. Sluiter, and H.W. Zandbergen: *Acta Mater.*, 2007, vol. 55, pp. 2183–99.
61. C.D. Marioara, S.J. Andersen, J. Jansen, and H.W. Zandbergen: *Acta Mater.*, 2001, vol. 49, pp. 321–28.
62. C.D. Marioara, S.J. Andersen, J. Jansen, and H.W. Zandbergen: *Acta Mater.*, 2003, vol. 51, pp. 789–96.
63. M.H. Mulazimoglu, A. Zaluska, F. Paray, and J.E. Gruzleski: *Metall. Mater. Trans. A*, 1997, vol. 28A, pp. 1289–95.
64. G.A. Edwards, K. Stiller, G.L. Dunlop, and M.J. Couper: *Acta Mater.*, 1998, vol. 46, pp. 3893–3904.
65. C.D. Marioara, S.J. Andersen, H.W. Zandbergen, and R. Holmestad: *Metall. Mater. Trans. A*, 2005, vol. 36A, pp. 691–702.
66. M. Murayama, K. Hono, M. Saga, and M. Kikuchi: *Mater. Sci. Eng. A*, 1998, vol. 250A, pp. 127–32.
67. A. Perovic, D.D. Perovic, G.C. Weatherly, and D.J. Lloyd: *Scripta Mater.*, 1999, vol. 41, pp. 703–08.

68. I. Dutta and D.L. Bourell: *Acta Metall. Mater.*, 1990, vol. 38, pp. 2041–49.
69. I. Dutta and S.M. Allen: *J. Mater. Sci. Lett.*, 1991, vol. 10, pp. 323–26.
70. A. Simar, Y. Brechet, B.D. Meester, A. Denquin, and T. Pardoen: *Mater. Sci. Eng. A*, 2008, vol. 486A, pp. 85–95.
71. R.W. Fonda and J.F. Bingert: *Metall. Mater. Trans. A*, 2004, vol. 35A, pp. 1487–99.
72. W.B. Lee, Y.M. Yeon, and S.B. Jung: *Mater. Sci. Technol.*, 2003, vol. 19, pp. 1513–18.
73. N. Afrin, D.L. Chen, X. Cao, and M. Jahazi: *Scripta Mater.*, 2007, vol. 57, pp. 1004–07.
74. N. Afrin, D.L. Chen, X. Cao, and M. Jahazi: *Mater. Sci. Eng. A*, 2008, vol. 472A, pp. 179–86.
75. N.E. Dowling: *Mechanical Behavior of Materials: Engineering Methods for Deformation, Fracture, and Fatigue*, 3rd ed., Pearson, Upper Saddle River, NJ, 2006.
76. A.M. Russell and K.L. Lee: *Structure-Property Relations in Non-ferrous Metals*, Wiley Interscience, New York, NY, 2005.
77. S. Lomolino, R. Tovo, and J.D. Santos: *Int. J. Fatigue*, 2005, vol. 27, pp. 305–16.
78. C. Laird: *Fatigue Crack Propagation*, ASTM STP 415, 1967, pp. 131–68.